Time-resolved high-energy X-ray diffraction studies of ultrathin Ni ferrite films on MgO(001)

Andreas Alexander,[a]* Tobias Pohlmann,[a,b] Martin Hoppe,[a,b] Jan Röh,[b] Olof Gutowski,[b] Karsten Küpper,[a] Florian Bertram[b] and Joachim Wollschläger[a]*

[a]Department of Physics, Osnabrück University, Barbarastraße 7, 49076 Osnabrück, Germany, and [b]Deutsches Elektronen-Synchrotron DESY, Notkestraße 85, 22607 Hamburg, Germany. *Correspondence e-mail: aalexander@uni-osnabrueck.de, jwollsch@uni-osnabrueck.de

Time-resolved high-energy X-ray diffraction was used during growth of ultrathin $Ni_xFe_{3-x}O_4$ films with varying Ni content ($0 \leq x \leq 1.5$) deposited on MgO(001) substrates by reactive molecular beam epitaxy, providing an insight into the growth dynamics of these films. In order to obtain structural information, reciprocal-space maps were recorded and the temporal evolution of the Bragg peaks specific to the octahedral and tetrahedral lattice sites of the inverse spinel structure of $Ni_xFe_{3-x}O_4$ was observed during growth of the films. A time delay, corresponding to a coverage of 1.2–1.8 nm, between the appearance of the Bragg reflections originating from octahedral sites and reflections originating exclusively from tetrahedral sites indicates that the ferrite films grow in two stages. In the initial growth phase, a rock salt interface layer is formed. Afterwards, a structural transition occurs and the films grow in an inverse spinel structure. The thickness of the initial rock salt phase was found to increase with Ni content and to be responsible for atypical strain in the thin films. Films with Ni contents $x > 1$ do not show a structural transition. These films remain in a (deficient) rock salt structure consisting of a mixed Ni–Fe oxide and do not form a spinel structure at all. They show an increased number of NiO clusters as detected by X-ray photoelectron spectroscopy of the valence band, accompanied by a significant roughening of the films.

1. Introduction

Transition metal ferrites are the focus of current research as a result of their special properties. For instance, high Curie temperatures and significant magnetic moments make most of them promising candidates for applications in the fields of spintronics (Hoffmann & Bader, 2015; Moussy, 2013; Cibert *et al.*, 2005), spincaloritronics (Bauer *et al.*, 2012) or electrocatalysis (Alshehri *et al.*, 2018; Kashyap & Kurungot, 2018), and as supercapacitors (Kumbhar *et al.*, 2012) or as high-capacity materials in lithium ion batteries (Li *et al.*, 2010; Chu *et al.*, 2004). For insulating ferrite films, one of these applications in the field of spintronics is as a spin filter capable of generating highly spin-polarized currents (Moyer *et al.*, 2015; Marnitz *et al.*, 2015; Matzen *et al.*, 2014, 2012; Moussy, 2013; Bibes & Barthelemy, 2007; Ramos *et al.*, 2007; Lüders *et al.*, 2006; Žutić *et al.*, 2004; Coey & Chien, 2003).

One promising material for such applications is $NiFe_2O_4$, an insulating and ferrimagnetic transition metal ferrite with a high Curie temperature of $T_C = 865$ K (Matzen *et al.*, 2014; Lüders *et al.*, 2006; Brabers, 1995).

As the spin filter efficiency and transmission of spin currents are highly dependent on the structural quality of the tunnelling barrier and its interfaces (Matzen *et al.*, 2014), it is crucial to grow ultrathin films with low defect densities for the manufacture of high-quality devices. Therefore, MgO(001) is
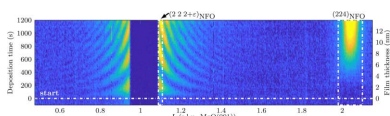
used as a substrate to minimize strain defects and disorder to allow pseudomorphic growth and obtain well ordered nickel ferrite structures, given its small lattice mismatch of 1% compared with $NiFe_2O_4$ and an O^{2-} face-centred cubic (f.c.c.) sublattice common to both oxides (Rodewald *et al.*, 2020; Chang *et al.*, 2016; Bertram *et al.*, 2013, 2012, 2011; Arora *et al.*, 2008; Tobin *et al.*, 2007; Tsymbal *et al.*, 2003; Margulies *et al.*, 1997).

Nevertheless, defects might occur during growth due to the rock salt structure of the MgO competing with the inverse spinel structure of the film, which can be described as an f.c.c. sublattice of O^{2-} (as mentioned above) and two cation sublattices with doubled periodicity compared with MgO. The Ni^{2+} cations are on lattice sites octahedrally coordinated by O^{2-} anions (B sites), while the Fe^{3+} cations are equally distributed on octahedrally (B sites) and tetrahedrally (A sites) coordinated sites. On the other hand, antiphase boundaries at the interface could be caused by the doubled lattice constant of the film compared with the substrate (Celotto *et al.*, 2003; Eerenstein *et al.*, 2003; Hibma *et al.*, 1999).

To steer the aforementioned properties, detailed knowledge of processes occurring during thin-film growth, especially in the very first growth stages, is necessary, since tunnelling barriers have a width of only a few nanometres. As the cationic ratio, *i.e.* the chemical composition, has a strong impact on structural, chemical, magnetic and electronic properties (de Biasi & dos Santos, 2017; Moyer *et al.*, 2012, 2011; Lenglet *et al.*, 1987), in this work, $Ni_xFe_{3-x}O_4$ (NFO) thin films with varying Ni contents in the range $0 \leq x \leq 1.5$ have been studied. The films were grown on MgO(001) by reactive molecular-beam epitaxy (RMBE). Note that the ferrite with $x = 0$ is magnetite, which is a half-metallic ferrimagnet having a Curie temperature of $T_C = 850$ K (Cornell & Schwertmann, 2003). The lattice constant of an Ni ferrite depends on its Ni content, as can be seen by comparing the bulk lattice constants of Fe_3O_4 (8.396 Å; Cornell & Schwertmann, 2003) and $NiFe_2O_4$ (8.339 Å; Liebermann, 1972) at room temperature. For instance, magnetite ($x = 0$) has a lattice mismatch of 0.3% compared with MgO.

To access the growth process directly, X-ray diffraction (XRD) experiments can be performed during deposition of the films (Rodewald *et al.*, 2020; Kuschel *et al.*, 2017). In this work, time-resolved high-energy X-ray diffraction (tr-HEXRD) was used to observe the temporal evolution of the Bragg peaks specific to the octahedral and tetrahedral lattice sites during growth of the NFO films to obtain structural information (Pohlmann *et al.*, 2022).

2. Experimental details

The growth dynamics of $Ni_xFe_{3-x}O_4$ thin films were studied by means of tr-HEXRD. The diffraction experiments were performed at the P07 beamline (EH2) of PETRA III at DESY in a specially designed ultra-high-vacuum (UHV) deposition chamber mounted on the heavy load diffractometer. Grazing-incidence diffraction was then performed during deposition (Pohlmann, 2021).

Table 1
Film thicknesses and deposition rates of the prepared samples.

The accuracy of the film thickness for all samples is ± 0.3 nm.

Ni content x	d_f (nm)	Rate (nm min^{-1})
0	8.3	0.21
0.2	18.8	2.81
0.6	9.1	0.61
1	13.9	0.70
1.3	12.4	1.24
1.5	8.2	0.41

Before deposition, the MgO(001) substrates were annealed for 1 h at 673 K in a molecular oxygen atmosphere of 1×10^{-4} mbar to clean the substrate from adsorbates and other contaminants (Kuepper *et al.*, 2016; Kuschel *et al.*, 2016). Afterwards, $Ni_xFe_{3-x}O_4$ thin films with varying Ni content (0 $\leq x \leq$ 1.5) were deposited by RMBE at a substrate temperature of 523 K in an oxygen atmosphere of 5×10^{-6} mbar. With this technique, Fe and Ni are evaporated simultaneously by electron bombardment of the respective pure metal target. The resulting molecular beams condense on the substrate surface and react to form an oxide film in the oxygen atmosphere. The growth rates and compositions of the ferrite films were steered by the fluxes of the individual evaporators. Table 1 summarizes the Ni content, final film thickness d_f and deposition rates of the six analysed samples.

For the diffraction experiment with a glancing angle of $\theta = 0.03°$, a photon energy of 71.5 keV was used and the data were collected by a Perkin–Elmer XRD 1621 2D area detector.

Before deposition, the cleaned samples were azimuthally aligned to an angle $\omega_{(11L)}$ to fulfil the Bragg condition for the (11L) crystal truncation rod (CTR) of the substrate. Here, L is defined by $L = q_\perp a_{MgO}/2\pi$, where $q_\perp$ denotes the component of the scattering vector **q** perpendicular to the film/substrate surface [$|\mathbf{q}| = (4\pi/\lambda)\sin\theta$, where θ is half the scattering angle and λ is the wavelength of the incident radiation] and $a_{MgO} = 421.2$ pm is the bulk lattice constant of MgO at room temperature. During deposition, the samples were continually rotated between $\omega_{(11L)} \pm 7°$ with a rotation speed of 2° s^{-1}. By this means, the diffraction signal was collected from the $(22L)_{NFO}$ CTR, which is close to $(11L)_{MgO}$ due to the small lattice mismatch. Afterwards, the detector images of these scans were summed in order to obtain a reciprocal-space map (RSM) every 10 s (Shipilin *et al.*, 2014).

After growth, the deposited film thickness was determined by means of X-ray reflectometry, and an RSM with a full 90° rotation at a speed of 0.25° s^{-1} was recorded to obtain a complete diffraction image of the film.

In order to probe the cation stoichiometry of the films, the electronic structure was characterized at Osnabrück University by X-ray photoelectron spectroscopy (XPS) after transport under ambient conditions. These studies were performed on a PHI VersaProbe III using a monochromated Al $K\alpha$ anode with a photon energy of E_{ph}(Al $K\alpha$) = 1486.6 eV. The cation stoichiometry was determined by integrating the intensities of both Fe 3p and Ni 3p.
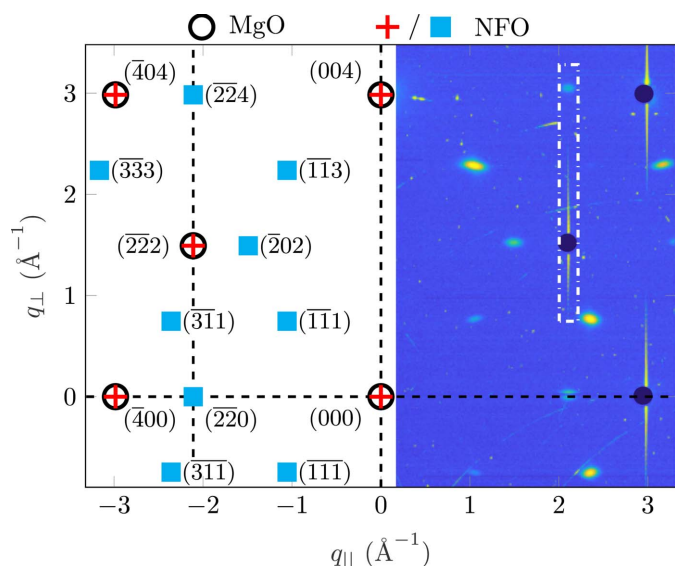
Figure 1
Full reciprocal-space map of the as-grown stoichiometric $NiFe_2O_4$ (NFO film with $x = 1$, film thickness 13.9 nm). The left-hand side shows schematically the expected Bragg positions for MgO and NFO. Because of the marginal difference between the two lattice constants, the lattice mismatch is neglected. The blue squares denote NFO reflections contributed by the A sublattice (tetrahedral cation sites) that are exclusive to the spinel structure, while the red crosses show the reflections contributed only by the B sublattice (octahedral cation sites) that are also allowed in a rock salt structure (open circles for MgO reflections). On the right-hand side, the white dashed box indicates the region of the $(22L)_{NFO}$ CTR including the $(224)_{NFO}$ Bragg reflection monitored in Fig. 2 for the evolution of intensity during growth. The dark regions at the positions of the substrate's reflections are beam stops protecting the detector from the bright Bragg reflections of the MgO substrate. Note the logarithmic intensity scale.

3. Results

Fig. 1 shows an RSM of the as-grown $NiFe_2O_4$ ($x = 1$) film with the expected Bragg positions for NFO and MgO.

One of the goals of this work was to record the temporal evolution of the intensities of the $(222)_{NFO}$ and $(224)_{NFO}$ reflections of the ferrite film to obtain information about the occupation of the tetrahedral and octahedral cation sites of the A and B sublattices, respectively. Due to the small lattice mismatch of 0.3–1% between MgO(001) and the halved lattice constant of NFO of varied Ni content, the Bragg reflections

$(HKL)_{MgO}$ of MgO and $(2H\ 2K\ 2L)_{NFO}$ of NFO almost coincide and cannot be separated. In addition, the intensity of the substrate reflections compared with the weaker film reflections is too high to be recorded simultaneously. Therefore, the substrate reflections have to be blocked by beamstops on the detector.

Due to the overlap of the $(222)_{NFO}$ reflection of the film and the substrate $(111)_{MgO}$ reflection which has to be blocked, this film reflection cannot be observed directly. Hence, the intensity of the CTR at the position $(2\ 2\ 2+\varepsilon)_{NFO}$ with $\varepsilon = 0.19$ was analysed (Pohlmann et al., 2022). In contrast, $(224)_{NFO}$ is fully visible, since the corresponding Bragg reflection $(112)_{MgO}$ of the substrate is forbidden due to the rock salt structure of MgO.

Fig. 2 shows a colour map of the intensity evolution along the $(22L)_{NFO}$ CTR during the growth process of the $NiFe_2O_4$ film. Before deposition started, no diffraction intensity corresponding to the film could be detected. As soon as deposition is started, Laue oscillations close to the $(222)_{NFO}$ Bragg reflection can be observed, indicating well ordered crystalline film growth. The period of the Laue fringes changes with increasing film thickness. The Laue fringes were fitted with Gaussians and their distance ΔL was used to determine the time-resolved film thickness d_f according to

$$\Delta L = a_{MgO}/d_f, \tag{1}$$

where a_{MgO} is the bulk lattice constant of the substrate (see inset in Fig. 3). For all samples a linear relation between deposition time and film thickness could be found, as shown in Fig. 3 for growth of $NiFe_2O_4$ ($x = 1$). This result clearly emphasizes that deposition was performed at a constant rate and the films grow layer by layer.

Immediately after the start of deposition, the intensity in the $(2\ 2\ 2+\varepsilon)_{NFO}$ region starts to oscillate due to evolving Laue fringes (Fig. 4). In contrast, $(224)_{NFO}$ is absent at the beginning, but it appears, after some delay, with increasing film thickness. This means that the octahedral sites are occupied immediately, while the tetrahedral sites are occupied with a delay.

Fig. 5 shows the critical film thicknesses for the onset of the Laue fringes close to $(222)_{NFO}$ and of the $(224)_{NFO}$ Bragg peaks for different cation stoichiometries.
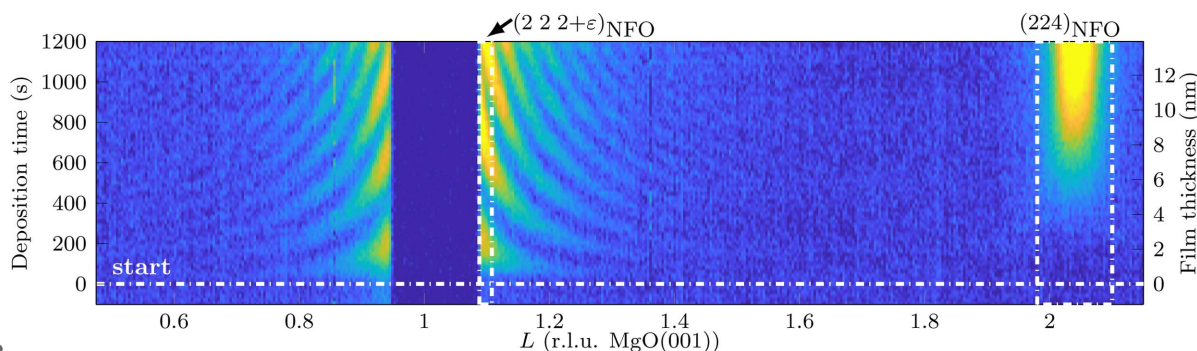

Figure 2
Evolution of the diffracted intensity along the $(22L)_{NFO}$ CTR, taken from the dashed box in Fig. 1 and presented for an Ni content of $x = 1$. The dashed horizontal white line indicates the start of deposition. The white dashed boxes show the regions where the intensities of $(224)_{NFO}$ and $(2\ 2\ 2+\varepsilon)_{NFO}$ were taken for their analysis. Note the logarithmic intensity scale.

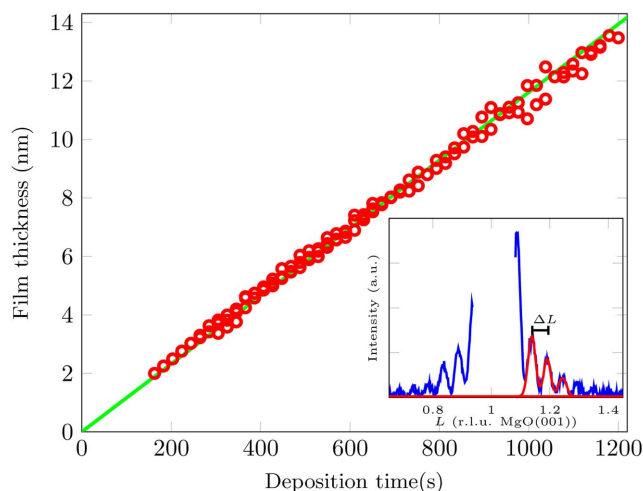**Figure 3**
Film thickness determined by Laue fringes (inset) as a function of deposition time, shown as an example for the growth of the NiFe$_2$O$_4$ film. There is a linear correlation between film thickness and deposition time. This observation is representative for the growth of all films. The inset shows the fitted Laue oscillations (red), and the derived distance ΔL was used to determine the film thickness d_f.
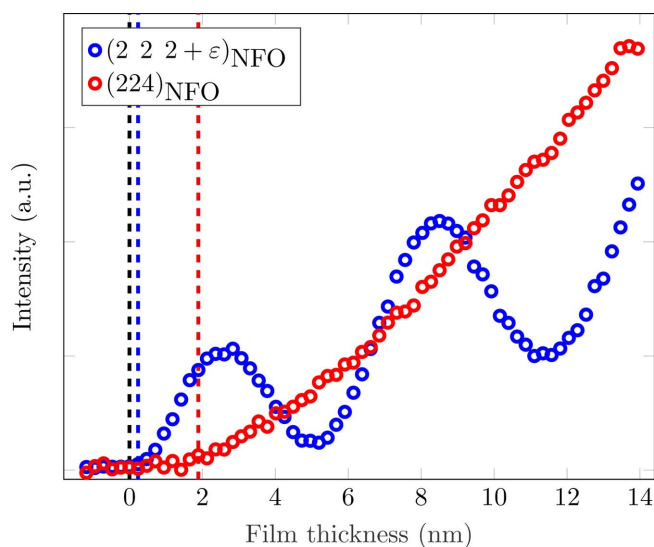

Figure 4
Intensity evolution of $(2\ 2\ 2+\varepsilon)_{NFO}$ and $(224)_{NFO}$ during deposition, shown for the NiFe$_2$O$_4$ film. The blue and red dashed lines indicate the film thickness where the intensities of $(2\ 2\ 2+\varepsilon)_{NFO}$ and $(224)_{NFO}$, respectively, start to appear. The black dashed line shows the time when the shutters of the evaporators were opened.

As mentioned before, for all samples the Laue fringes of $(222)_{NFO}$ related to $(2\ 2\ 2+\varepsilon)_{NFO}$ appear immediately after the start of deposition. The intensity rise in $(224)_{NFO}$ is delayed by 1.23 (4) nm for Fe$_3$O$_4$ (NFO with $x = 0$). This delay increases with Ni content up to $x = 1$. For higher Ni content ($x > 1$), $(224)_{NFO}$ was not visible at all, indicating that no spinel structure has formed and the oxide film has an apparent rock salt structure without occupation of A cation sites or with a strong disorder on the A cation sites.

In order to obtain qualitative information about the roughening of the film, the evolution in the intensity of one
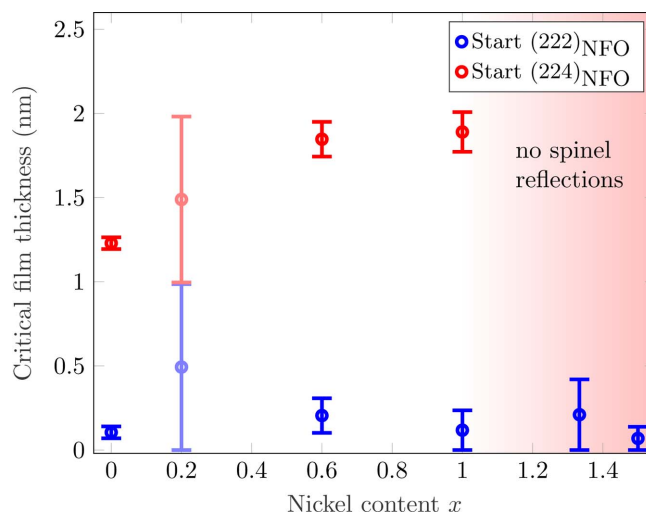

Figure 5
Critical film thickness for the onset of the evolution of the $(2\ 2\ 2+\varepsilon)_{NFO}$ (red data points) and $(224)_{NFO}$ (blue data points) intensities for different Ni contents. Above an Ni content of $x = 1$ no formation of $(224)_{NFO}$ could be observed, indicating that no ordered spinel structure has formed. The large uncertainty for $x = 0.2$ (transparent) is due to the high deposition rate and the resulting poor thickness resolution, so these data should be considered with caution (Table 1).

specific Laue fringe (second order) was analysed [inset in Fig. 6(a)]. Assuming an ideal smooth surface, the intensity of the Laue oscillations can be described by the N-slit function,

$$I \propto \frac{\sin^2(Ncq_\perp/2)}{\sin^2(cq_\perp/2)}, \qquad (2)$$

with the out-of-plane scattering vector component $q_\perp$, the layer distance c and the number of layers N (Robinson & Tweet, 1992). With $d_f = Nc$ being the film thickness and assuming that a maximum is approximately in the centre between two minima, the position of the nth order maximum can be approximated by

$$q_\perp \simeq \frac{2\pi(n+1/2)}{d_f}. \qquad (3)$$

Thus, the intensity for an nth-order maximum is given as

$$I_n \propto \frac{1}{\left[(\pi c/d_f)(n+1/2)\right]^2}. \qquad (4)$$

Hence, the quotient of the intensity and the square of the film thickness,

$$\frac{I_n}{d_f^2} \propto \frac{1}{\left[\pi c(n+1/2)\right]^2} = \text{constant}, \qquad (5)$$

should remain constant for an ideal smooth surface/interface. Any deviation from a constant behaviour for the growing film with evolving film thickness is due to a change in roughness of the surface or interface of the film during growth. Thus, a variation in this quotient points to roughening of the film. As seen in Fig. 6(a), this variation can be approximated by a linear function,
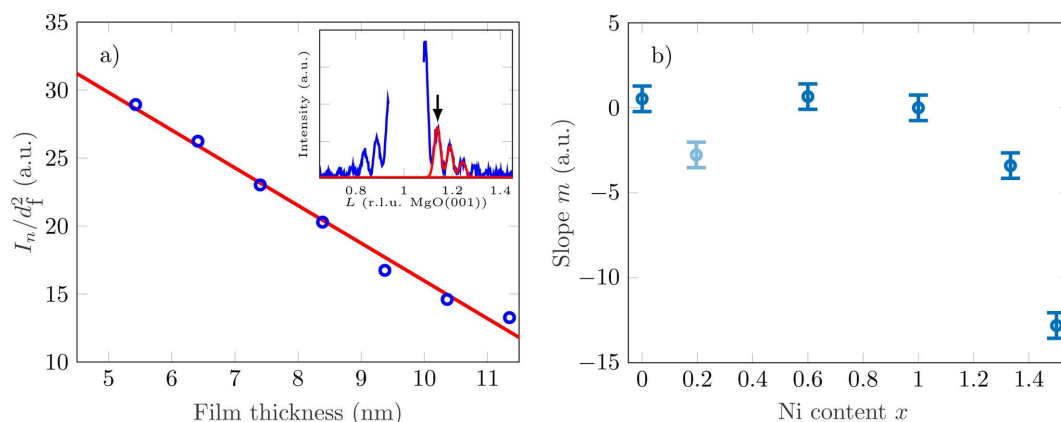
Figure 6
(*a*) The quotient of intensity of the *n*th Laue fringe (here *n* = 2) and the squared film thickness as a function of film thickness, shown for the NFO film with *x* = 0.2. The red line shows the fitted linearly decreasing intensity of the Laue fringe. The inset shows the fitted Laue oscillations (red), the arrow pointing to the analysed second-order Laue fringe. (*b*) Slopes *m* for the different Ni contents. The data for Ni content *x* = 0.2 (transparent) should only be compared with other data with caution because of the different deposition rate (Table 1).

$$\Delta \frac{I_n}{d_f^2} = m \, \Delta d_f. \qquad (6)$$

The slope *m* of this approximation can be used as a measure of the roughness.

Fig. 6(*b*) shows the slope *m* of this quotient for different cation stoichiometries. For films with an Ni content of $x \leq 1$, there is no significant variation in the quotient [equation (5)] of the intensity and the square of the film thickness, indicating no increase in roughness with increasing film thickness. Only the film with *x* = 0.2 shows a slope related to an increase in roughening, which can be explained by structural disorder as a result of a significantly higher deposition rate (Table 1). For overstoichiometric NFO films (*x* > 1) the slope decreases with increasing Ni content, which means more roughening of the layer with increasing film thickness. This could be explained by the fact that no ordered spinel structure could be formed, either due to a disorder of the *A* sublattice or due to intermixing rock salt phases.

To obtain information about the temporal evolution of the vertical and lateral layer distances during growth, the position in reciprocal space of the $(113)_{NFO}$ reflection of the film was determined, since it is the measured reflection with the highest intensity and does not coincide with a Bragg reflection of the substrate. Therefore, the Bragg peak was fitted with a 2D Gaussian to obtain both the out-of-plane and in-plane positions. Overstoichiometric films (*x* > 1) did not show the $(113)_{NFO}$ reflection due to their apparent rock salt structure (see above). Therefore, we used the interpolated position of $(222)_{NFO}$ to determine the temporal evolution of the lattice constants of these growing films. The lateral position was determined by fitting the $(2\,2\,1.88)_{NFO}$ CTR and the vertical position by interpolation of the corresponding Laue fringes (inset in Fig. 7). Fig. 7 shows a comparison of these two fitting methods for the $NiFe_2O_4$ film where both Bragg peaks $(113)_{NFO}$ and $(222)_{NFO}$ are present. Despite a worse signal-to-noise-ratio for $(222)_{NFO}$, the two methods provide the same values for the layer distances, confirming the validity of the approach.

Fig. 8(*a*) shows the temporal evolution of the lateral and vertical layer distances for different Ni contents obtained from this analysis. For films with an Ni content up to *x* = 1 with evolving spinel structure, both the lateral and the vertical layer distances move from higher to lower values, corresponding to a decreasing expansion in the lateral direction and an increasing compression in the vertical direction with increasing film thickness. The relaxation of the lateral layer distance is much smaller than that of the vertical layer distance. For overstoichiometric films (*x* > 1) with the apparent rock salt structure, there is a slight decrease in the lateral direction and an increase in the vertical layer distance with increasing film thickness, corresponding to a decreasing compression and slightly decreasing expansion in the vertical and lateral directions, respectively. The dashed lines in Fig. 8 correspond to the layer distances expected for bulk FeO, MgO,
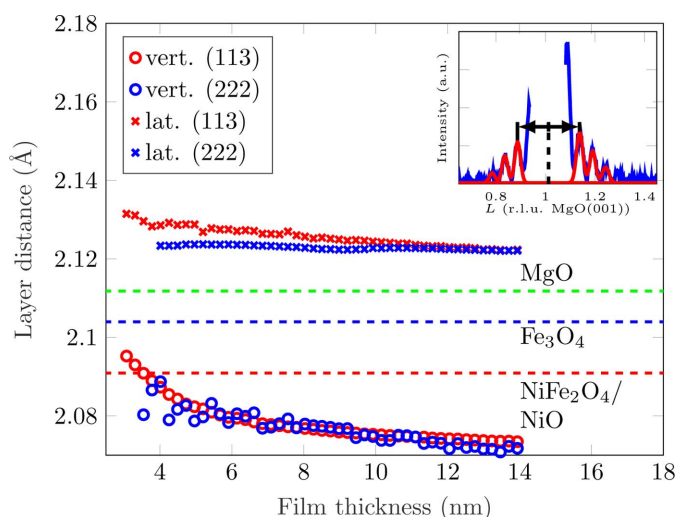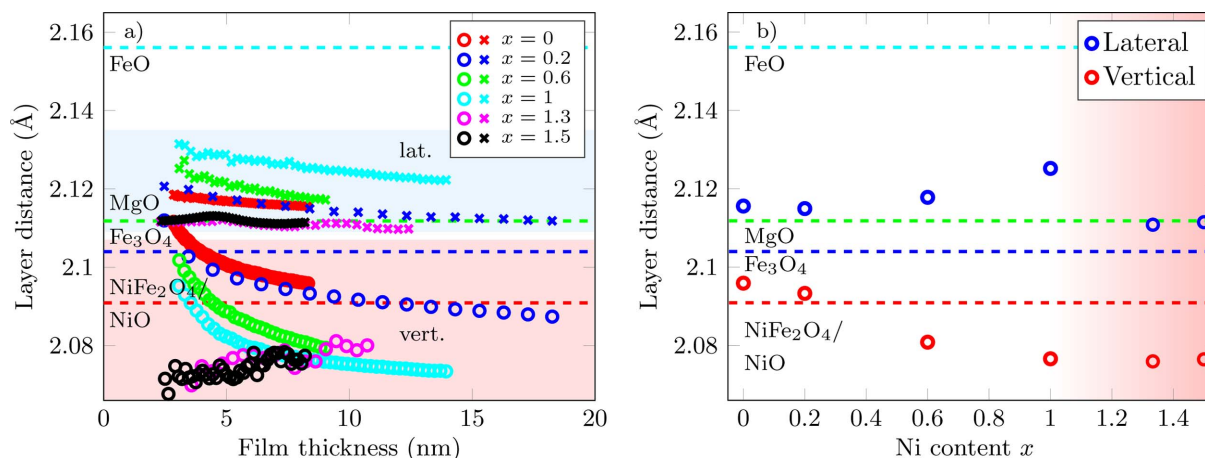

Figure 7
Comparison of the two fitting methods used for the determination of layer distances, shown for the $NiFe_2O_4$ film. The expected bulk values for MgO, Fe_3O_4, $NiFe_2O_4$ and NiO at the deposition temperature of 526 K are indicated by dashed lines. The inset shows a schematic representation of the interpolation by fitting the oscillations with Gaussians (red line) and calculating the mid-point of symmetrically equivalent fringes.
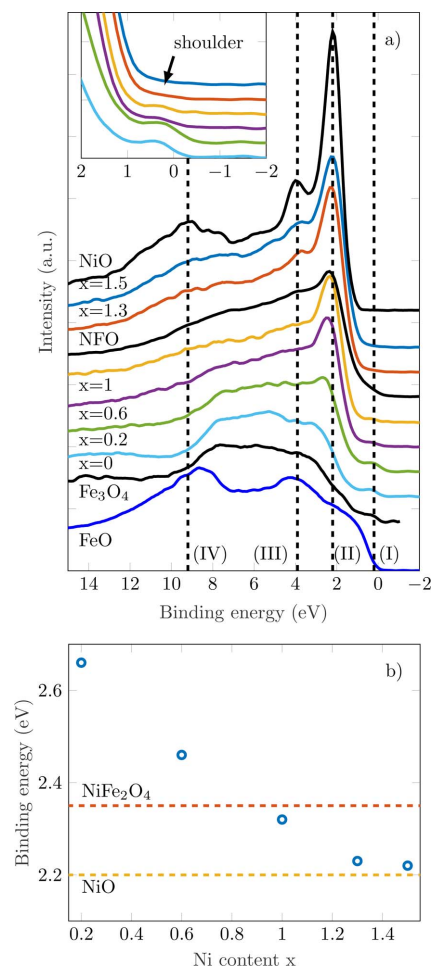
Figure 8
(*a*) Evolution of the lateral (crosses) and vertical (circles) layer distances for different Ni contents, determined by fitting of $(113)_{NFO}$ for films with an Ni content up to $x = 1$. The layer parameters for the overstoichiometric films ($x > 1$) were taken from the interpolation of the $(222)_{NFO}$ Laue fringes. (*b*) The lateral and vertical layer distances for different Ni contents at a film thickness of $d_f = 8.25$ (7) nm. The expected bulk values for FeO, MgO, Fe_3O_4, $NiFe_2O_4$ and NiO at the deposition temperature of 523 K are indicated by dashed lines.

Fe_3O_4, $NiFe_2O_4$ and NiO at the deposition temperature of 523 K, determined by their respective thermal expansion coefficients (Nelson *et al.*, 2014; Levy *et al.*, 2004; Touloukian *et al.*, 1977).

The lateral layer distances of the NFO films are slightly higher than the expected value for pseudomorphic growth on bulk MgO(001), while the vertical distances tend to be smaller than the expected layer distance for bulk Fe_3O_4 and $NiFe_2O_4$/NiO, which is expected for tetragonally distorted films (Hashimoto *et al.*, 1985). Fig. 8(*b*) shows the layer distances c for different cation stoichiometries at a film thickness of 8.25 (7) nm. It can be seen that, for the films with an Ni content up to $x = 1$, the lateral layer distances, starting at the bulk value for MgO, increase with increasing Ni content x. The lateral layer distance of the overstoichiometric films, however, returns to the lattice distance of MgO. The vertical lattice distances decrease from slightly below the expected bulk value for Fe_3O_4 to below the bulk value of $NiFe_2O_4$ and/or NiO. Thus, the films are vertically compressed.

To probe the electronic structure, the valence band of the NFO films was analysed by means of XPS performed *a posteriori* and compared with reference XPS spectra for FeO, Fe_3O_4, $NiFe_2O_4$ and NiO [Fig. 9(*a*)]. Since none of the measured spectra show similarities with the reference spectrum of FeO, this indicates that no wustite was formed in large amounts. As expected, the spectrum of the NFO film with $x = 0$ (magnetite) matches very well with the reference spectrum for Fe_3O_4. In particular, the feature labelled (I) at about 0.2 eV binding energy is characteristic of magnetite and comes from Fe^{2+} ions on octahedrally coordinated cation sites (Paul, 2010). The spectra for the unstoichiometric NFO films ($0 < x < 1$) are a superposition of the spectra of both magnetite and $NiFe_2O_4$. The disappearance of the characteristic shoulder (I) with increasing Ni content x indicates that the Fe^{2+} cations are replaced by Ni^{2+} ions. Obviously, electronic states at the Fermi edge are increasingly suppressed, pointing to a transition from half-metallic Fe_3O_4 to insulating $NiFe_2O_4$. The spectrum of the $NiFe_2O_4$ film (NFO with $x = 1$) shows strong similarities to the

Figure 9
(*a*) X-ray photoelectron spectra of the valence band of all $Ni_xFe_{3-x}O_4$ films and reference spectra for FeO, Fe_3O_4, $NiFe_2O_4$ and NiO. For better comparison the spectra are shifted. The positions labelled (I), (II), (III) and (IV) denote characteristic features of the respective films. The inset shows an enlargement of the low binding energy region close to the Fermi edge. (*b*) The positions of feature (II) for the different NFO films (blue circles) with the expected peak positions for $NiFe_2O_4$ and NiO (dashed lines).

reference spectrum but also shows feature (I) originating from Fe^{2+} ions on B sites. This means that not all Fe^{2+} cations are replaced by Ni^{2+} ions or that there is no perfect inverse spinel structure of the film ('inversion defect').

Since the overstoichiometric films show the characteristic features (II), (III) and (V) of NiO, it is evident that NiO, or an intermixing of NiO and a nickel–iron oxide rock salt structure, has formed in these films. The energy shift of the Ni peak [feature (II)] from the expected position for $NiFe_2O_4$ to the expected values for NiO with increasing Ni content [Fig. 9(b)] agrees with the result that, for Ni contents of $x > 1$, clusters of NiO are formed embedded in a (deficient) rock salt matrix (Bertram *et al.*, 2013).

4. Discussion

While the intensity of the $(222)_{NFO}$ reflection has contributions from both oxygen and cations on the B sublattice (octahedral sites), occurring also in the rock salt structure, the $(224)_{NFO}$ reflection only has a contribution from the A cation sublattice (tetrahedral), which is exclusive to the spinel structure (Bertram *et al.*, 2013). The $(222)_{NFO}$ reflection appears immediately after the start of deposition, while the formation of the $(224)_{NFO}$ reflection follows with a delay for Ni contents $x \leq 1$. This result indicates that in the very first growth stages either the film grows in a rock salt structure $Ni_yFe_{1-y}O$ (with $y = x/3$) with only the octahedral sites occupied, instead of an (inverse) spinel structure, or the A sublattice is heavily disordered. It is also possible that, initially, a deficient rock salt structure is formed by the NiFe oxide, where A sites are unoccupied and only 3/4 of the B sites are occupied by cations (Bertram *et al.*, 2013). After this initial growth stage, a structural transition occurs and the spinel structure starts to form, as already observed for Fe_3O_4 (Pohlmann *et al.*, 2022; Bertram *et al.*, 2012). The thickness of this initial growth phase was determined to be 1.2–1.8 nm, corresponding to about three or four (rock salt) unit cells or about six to eight atomic layers of FeO or NiO.

For higher Ni contents $x > 1$, the formation of a spinel structure is not observed at all and the films have the rock salt structure $Ni_yFe_{1-y}O$ or a deficient rock salt structure. Thus, for $1 < x < 1.3$ there is a critical Ni content where no spinel structure can be formed. This result is also supported by the XPS measurements of the valence band, showing that NiO is formed for $x > 1$, which crystallizes in a rock salt structure. Hence, one can assume that the films consist of different phases as clusters of NiO embedded in an $Ni_yFe_{1-y}O$ rock salt matrix or in a deficient rock salt structure.

The roughening of the surface increases with increasing film thickness and Ni content for $x > 1$. This behaviour is also observed for the film with $x = 0.2$, which was grown with a significantly higher deposition rate. This critical stoichiometry for the film roughening correlates with the transition from spinel to apparent rock salt structure. This could be due to competition between the spinel NFO structure and the (deficient) rock salt $Ni_yFe_{1-y}O$ structure, or to a roughness related to disorder of the A sublattice, which also affects the interface.

While these overstoichiometric films ($x > 1$) show a lateral film-thickness-independent expansion towards the layer distance of MgO and a vertical compression compared with the expected bulk lattice constant, as is expected for pseudomorphic growth, films with Ni contents of $x \leq 1$ show behaviour not expected from classical growth theory. As the obtained lateral layer distance is larger than that of MgO, the tensile strain on the NFO films has to be much higher. This effect was already observed by Kuschel *et al.* (2018) for the growth of magnetite on an NiO interlayer pseudomorphic to the MgO(001) substrate and could be attributed to the formation of antiphase boundaries (APBs). Thus, we conclude that this effect also appears here at the interface of NFO and MgO, since the lattice constant of NFO is roughly twice as large as that of the substrate. Accordingly, the additional tensile strain induced by APBs increases at a higher Ni content, caused by the higher lattice mismatch of $NiFe_2O_4$ to MgO versus Fe_3O_4 to MgO [Fig. 8(b)]. Assuming the rock salt structure for overstoichiometric films, it is evident that no APBs are formed and pseudomorphic growth occurs.

A similar observation can be found in the relaxation behaviour of the NFO films. The overstoichiometric films with apparent rock salt structure show decreasing compression in the vertical direction and slightly decreasing expansion in the lateral direction with increasing film thickness, which is expected for (quasi-)pseudomorphic growth of NFO or NiO on MgO and supports the assumption of the deficient rock salt structure. In contrast, the NFO films with Ni contents of $x \leq 1$ show decreasing expansion and increasing compression for the lateral and vertical directions, respectively, so pseudomorphic growth of NFO on MgO cannot be assumed for these films. A similar behaviour was observed by Bertram *et al.* (2012) for Fe_3O_4 grown on MgO at room temperature. This effect is assumed to be due to the initial rock salt interface layer, which could be induced by the rock salt structure of the substrate. Another explanation could be a deficit of oxygen in the initial growth phase. Oxygen vacancies in the substrate due to the preparation regime could bind oxygen from the film, resulting in a deficient rock salt structure at the interface consisting of an intermixing wustite and NiO film (Bertram *et al.*, 2013).

5. Summary

In conclusion, ultrathin $Ni_xFe_{3-x}O_4$ films with varying Ni content ($0 \leq x \leq 1.5$) were grown by RMBE. Using tr-HEXRD during deposition provides insight into the growth dynamics of these films. It was found that NFO films grow in two stages. At first, the films start to grow in a rock salt phase. Then, after a coverage of 1.2–1.8 nm, a structural transition occurs and the films grow in an inverse spinel structure for Ni contents $x \leq 1$. The thickness of the interface layer formed during the initial growth phase, responsible for atypical strain in the NFO film, increases with Ni content. However, this transition could only be observed for films with a maximum Ni content of $x = 1$. Overstoichiometric films did not form a spinel structure and remained in a rock salt structure. Valence band spectra show that the densities of states at the Fermi edge are

reduced with increasing Ni content. Thus, one needs high Ni content to obtain the insulating Ni ferrite films that are necessary for application as spin filters.

References

Alshehri, S. M., Alhabarah, A. N., Ahmed, J., Naushad, M. & Ahamad, T. (2018). *J. Colloid Interface Sci.* **514**, 1–9.

Arora, S. K., Wu, H.-C., Yao, H., Ching, W. Y., Choudhary, R. J., Shvets, I. V. & Mryasov, O. N. (2008). *IEEE Trans. Magn.* **44**, 2628–2631.

Bauer, G. E. W., Saitoh, E. & van Wees, B. J. (2012). *Nat. Mater.* **11**, 391–399.

Bertram, F., Deiter, C., Hoefert, O., Schemme, T., Timmer, F., Suendorf, M., Zimmermann, B. & Wollschläger, J. (2012). *J. Phys. D Appl. Phys.* **45**, 395302.

Bertram, F., Deiter, C., Pflaum, K., Suendorf, M., Otte, C. & Wollschläger, J. (2011). *J. Appl. Phys.* **110**, 102208.

Bertram, F., Deiter, C., Schemme, T., Jentsch, S. & Wollschläger, J. (2013). *J. Appl. Phys.* **113**, 184103.

Biasi, R. S. de & dos Santos, H. (2017). *Ceram. Int.* **43**, 4557–4561.

Bibes, M. & Barthelemy, A. (2007). *IEEE Trans. Electron Devices*, **54**, 1003–1023.

Brabers, V. A. M. (1995). *Handbook of Magnetic Materials*, pp. 189–324. Amsterdam: Elsevier.

Celotto, S., Eerenstein, W. & Hibma, T. (2003). *Eur. Phys. J. B*, **36**, 271–279.

Chang, C., Hu, Z., Klein, S., Liu, X., Sutarto, R., Tanaka, A., Cezar, J., Brookes, N., Lin, H.-J., Hsieh, H., Chen, C., Rata, A. & Tjeng, L. (2016). *Phys. Rev. X*, **6**, 041011.

Chu, Y.-Q., Fu, Z.-W. & Qin, Q.-Z. (2004). *Electrochim. Acta*, **49**, 4915–4921.

Cibert, J., Bobo, J.-F. & Lüders, U. (2005). *C. R. Phys.* **6**, 977–996.

Coey, J. M. D. & Chien, C. L. (2003). *MRS Bull.* **28**, 720–724.

Cornell, R. M. & Schwertmann, U. (2003). *The Iron Oxides: Structure, Properties, Reactions, Occurences and Uses.* Weinheim: Wiley-VCH Verlag GmbH.

Eerenstein, W., Palstra, T. T. M., Hibma, T. & Celotto, S. (2003). *Phys. Rev. B*, **68**, 014428.

Hashimoto, S., Peng, J.-L., Gibson, W. M., Schowalter, L. J. & Fathauer, R. W. (1985). *Appl. Phys. Lett.* **47**, 1071–1073.

Hibma, T., Voogt, F. C., Niesen, L., van der Heijden, P. A. A., de Jonge, W. J. M., Donkers, J. J. T. M. & van der Zaag, P. J. (1999). *J. Appl. Phys.* **85**, 5291–5293.

Hoffmann, A. & Bader, S. D. (2015). *Phys. Rev. Appl.* **4**, 047001.

Kashyap, V. & Kurungot, S. (2018). *ACS Catal.* **8**, 3715–3726.

Kuepper, K., Kuschel, O., Pathé, N., Schemme, T., Schmalhorst, J., Thomas, A., Arenholz, E., Gorgoi, M., Ovsyannikov, R., Bartkowski, S., Reiss, G. & Wollschläger, J. (2016). *Phys. Rev. B*, **94**, 024401.

Kumbhar, V. S., Jagadale, A. D., Shinde, N. M. & Lokhande, C. D. (2012). *Appl. Surf. Sci.* **259**, 39–43.

Kuschel, O., Buß, R., Spiess, W., Schemme, T., Wöllermann, J., Balinski, K., N'Diaye, A. T., Kuschel, T., Wollschläger, J. & Kuepper, K. (2016). *Phys. Rev. B*, **94**, 094423.

Kuschel, O., Pathé, N., Schemme, T., Ruwisch, K., Rodewald, J., Buss, R., Bertram, F., Kuschel, T., Kuepper, K. & Wollschläger, J. (2018). *Materials*, **11**, 1122.

Kuschel, O., Spiess, W., Schemme, T., Rubio-Zuazo, J., Kuepper, K. & Wollschläger, J. (2017). *Appl. Phys. Lett.* **111**, 041902.

Lenglet, M., D'Huysser, A. & Jørgensen, C. K. (1987). *Inorg. Chim. Acta*, **133**, 61–65.

Levy, D., Artioli, G. & Dapiaggi, M. (2004). *J. Solid State Chem.* **177**, 1713–1716.

Li, Z. H., Zhao, T. P., Zhan, X. Y., Gao, D. S., Xiao, Q. Z. & Lei, G. T. (2010). *Electrochim. Acta*, **55**, 4594–4598.

Liebermann, R. C. (1972). *Phys. Earth Planet. Inter.* **6**, 360–365.

Lüders, U., Barthélémy, A., Bibes, M., Bouzehouane, K., Fusil, S., Jacquet, E., Contour, J.-P., Bobo, J.-F., Fontcuberta, J. & Fert, A. (2006). *Adv. Mater.* **18**, 1733–1736.

Margulies, D. T., Parker, F. T., Rudee, M. L., Spada, F. E., Chapman, J. N., Aitchison, P. R. & Berkowitz, A. E. (1997). *Phys. Rev. Lett.* **79**, 5162–5165.

Marnitz, L., Rott, K., Niehörster, S., Klewe, C., Meier, D., Fabretti, S., Witziok, M., Krampf, A., Kuschel, O., Schemme, T., Kuepper, K., Wollschläger, J., Thomas, A., Reiss, G. & Kuschel, T. (2015). *AIP Advances*, **5**, 047103.

Matzen, S., Moussy, J.-B., Mattana, R., Bouzehouane, K., Deranlot, C. & Petroff, F. (2012). *Appl. Phys. Lett.* **101**, 042409.

Matzen, S., Moussy, J.-B., Wei, P., Gatel, C., Cezar, J. C., Arrio, M. A., Sainctavit, P. & Moodera, J. S. (2014). *Appl. Phys. Lett.* **104**, 182404.

Moussy, J.-B. (2013). *J. Phys. D Appl. Phys.* **46**, 143001.

Moyer, J. A., Gao, R., Schiffer, P. & Martin, L. W. (2015). *Sci. Rep.* **5**, 10363.

Moyer, J. A., Kumah, D. P., Vaz, C. A. F., Arena, D. A. & Henrich, V. E. (2012). *Appl. Phys. Lett.* **101**, 021907.

Moyer, J. A., Vaz, C. A. F., Negusse, E., Arena, D. A. & Henrich, V. E. (2011). *Phys. Rev. B*, **83**, 035121.

Nelson, A. T., White, J. T., Andersson, D. A., Aguiar, J. A., McClellan, K. J., Byler, D. D., Short, M. P. & Stanek, C. R. (2014). *J. Am. Ceram. Soc.* **97**, 1559–1565.

Paul, M. C. (2010). PhD thesis, University of Würzburg, Germany.

Pohlmann, T. (2021). PhD thesis, Osnabrück University, Germany.

Pohlmann, T., Hoppe, M., Thien, J., Dey, A. B., Alexander, A., Ruwisch, K., Gutowski, O., Röh, J., Gloskovskii, A., Schlueter, C., Küpper, K., Wollschläger, J. & Bertram, F. (2022). *Phys. Rev. B*, **105**, 045412.

Ramos, A. V., Guittet, M.-J., Moussy, J.-B., Mattana, R., Deranlot, C., Petroff, F. & Gatel, C. (2007). *Appl. Phys. Lett.* **91**, 122107.

Robinson, I. K. & Tweet, D. J. (1992). *Rep. Prog. Phys.* **55**, 599–651.

Rodewald, J., Thien, J., Pohlmann, T., Hoppe, M., Bertram, F., Kuepper, K. & Wollschläger, J. (2020). *Appl. Phys. Lett.* **117**, 011601.

Shipilin, M., Hejral, U., Lundgren, E., Merte, L. R., Zhang, C., Stierle, A., Ruett, U., Gutowski, O., Skoglundh, M., Carlsson, P.-A. & Gustafson, J. (2014). *Surf. Sci.* **630**, 229–235.

Tobin, J. G., Morton, S. A., Yu, S. W., Waddill, G. D., Schuller, I. K. & Chambers, S. A. (2007). *J. Phys. Condens. Matter*, **19**, 315218.

Touloukian, Y. S., Kirby, R. K., Taylor, E. R. & Lee, T. Y. R. (1977). *Thermophysical Properties of Matter*, The TPRC Data Series, Vol. 13, *Thermal Expansion – Nonmetallic Solids.* Defense Technical Information Center, Fort Belvoir, Virginia, USA.

Tsymbal, E. Y., Mryasov, O. N. & LeClair, P. R. (2003). *J. Phys. Condens. Matter*, **15**, R109–R142.

Žutić, I., Fabian, J. & Sarma, S. D. (2004). *Rev. Mod. Phys.* **76**, 323–410.